Experimental evidence for wall-rock pulverization during dynamic rupture at ultra-high pressure conditions

Sarah Incel, Alexandre Schubnel, Jörg Renner, Timm John, Loïc Labrousse, Nadege Hilairet, Helen Freeman, Yanbin Wang, François Renard, Bjørn Jamtveit

Experimental evidence for wall rock pulverization during dynamic rupture at ultra-high pressure conditions

Sarah Incel[1], Alexandre Schubnel[2], Jörg Renner[3], Timm John[4], Loïc Labrousse[5], Nadège Hilairet[6], Helen Freeman[7], Yanbin Wang[8], François Renard[1,9], and Bjørn Jamtveit[1]

[1]Physics of Geological Processes, The Njord Centre, Department of Geosciences, University of Oslo, Box 1048 Blindern, 0316 Oslo, Norway

[2]Laboratoire de Géologie de l'ENS - PSL Research University - UMR8538 du CNRS, 24 Rue Lhomond, 75005 Paris, France

[3]Ruhr-Universität Bochum, Universitätsstraße 150, 44801 Bochum, Germany

[4]Freie Universität Berlin, Institute of Geological Sciences, Malteserstr. 74-100, 12249 Berlin, Germany

[5]Sorbonne Université, CNRS-INSU, Institut des Sciences de la Terre Paris, ISTeP, UMR 7193, 75005 Paris, France

[6]Univ. Lille, CNRS, INRA, ENSCL, UMR 8207 - Unité Matériaux et Transformations, 59000 Lille, France

[7]Helmholtz-Zentrum Potsdam, Deutsches GeoForschungsZentrum GFZ, Telegrafenberg, 14473 Potsdam, Germany

[8]Center for Advanced Radiation Sources, the University of Chicago, Chicago, IL 60637, USA

[9]Univ. Grenoble Alpes, Univ. Savoie Mont Blanc, CNRS, IRD, IFSTTAR, ISTerre, 38000 Grenoble, France

*Correspondence to: sarah.incel@gmail.com

Abstract

The mechanisms triggering intermediate and deep earthquakes have puzzled geologists for several decades. There is still no consensus concerning whether such earthquakes are triggered by brittle or ductile mechanisms. We performed a deformation experiment on a synthetic lawsonite-bearing blueschist at a confining pressure of 3 GPa and temperatures from 583 to 1,073 K. After deformation, the recovered sample reveals conjugated shear fractures. Garnet crystals are dissected and displaced along these narrow faults and reveal micro- and nanostructures that resemble natural pulverization structures as well as partial amorphization. Formation of such structures is known to require strain rates exceeding 10^2 s^{-1} at low confining pressures and is explained by the propagation of a dynamic shear rupture. The absence of shearing in the pulverized wall rock is taken as evidence that these structures pre-date the subsequent heat-producing frictional slip. In analogy to observations at low pressure we infer that the garnet structures in our experiment result from rapid propagation of a shear fracture even at the high pressure exerted on the sample and thus suggest that brittle deformation is possible at lower crustal to upper mantle depths.

Keywords: pulverization, high-pressure deformation, dynamic rupture, lawsonite-blueschist, DDIA apparatus, acoustic emissions

1. Introduction

During subduction at convergent plate margins, intermediate depth (70-300 km) and deep (>300 km) earthquakes are common. Yet, the processes triggering earthquakes at the high pressures (>1 GPa) prevailing at these depths are poorly understood. Both brittle (Raleigh and Paterson, 1965; Kirby, 1987; Green II and Burnley, 1989; Dobson et al., 2002; Hacker et al.,

47 2003b; Schubnel et al., 2013; Okazaki and Hirth, 2016; Ferrand et al., 2017; Gasc et al., 2017;
48 Incel et al., 2017, 2019; and references therein) and ductile (Braeck and Podladchikov, 2007;
49 Kelemen and Hirth, 2007; John et al., 2009; Thielmann et al., 2015; Poli and Prieto, 2016;
50 Prieto et al., 2017; and references therein) mechanisms have been proposed.

51 While the suggested ductile mechanisms involve self-localizing failure by dissipative
52 heating and thermal runaway situations, the considered brittle mechanisms involve dynamic
53 rupture. In the former case, one expects significant shear deformation prior to seismic slip,
54 whereas in the latter case, wall rock damage may occur due to high strain rates and rapidly
55 changing stresses near a propagating rupture tip prior to frictional heating of the shear fracture
56 surfaces (Ben-Zion, 2003). Wall rock deformation associated with paleaoearthquakes inferred
57 from the presence of pseudotchylytes, a rock type often assumed to be the result of frictional
58 melting and subsequent quenching (McKenzie and Brune, 1972; Sibson, 1975), was
59 interpreted as evidence for a thermal runaway mechanism (John et al., 2009; Deseta et al.,
60 2014). Studies of pseudotachylyte veins and their surrounding wall rocks in naturally
61 deformed rocks do, however, pose a number of challenges due to postseismic deformation and
62 recovery processes with respect to their formation (Guermani and Pennacchioni, 1998;
63 Mancktelow, 2006; Kirkpatrick and Rowe, 2013). Recent microstrutural observations indicate
64 extremely high stresses in wall rocks around lower crustal earthquake zones, and abundant
65 fragmentation (Angiboust et al., 2012) without observable shear (Austrheim et al., 2017;
66 Petley-Ragan et al., 2018). Such fragmentation is often referred to as ‘pulverization’ when
67 occuring around faults in the shallow seismogenic regime and is assumed to result from
68 dynamic rupture processes (Dor et al., 2006; Mitchell and Faulkner, 2009; Rempe et al.,
69 2013).

70 In a previous experimental study, synthetic polycrystalline lawsonite-bearing blueschist
71 samples were deformed at confining pressures corresponding to lower crustal to upper mantle

depths (Incel et al. 2017). Faulting was accompanied by the record of acoustic emissions and the growth of eclogite-facies minerals monitored using in-situ powder diffraction. Examination of the recovered run products revealed several conjugated faults decorated with nanocrystalline ecologite-facies transformation products in samples that entered the stability field of eclogite. Therefore, Incel et al. (2017) suggested that failure occurred due to transformation-induced instabilities, a mechanism titled transformational faulting (see also Kirby, 1987; Green II and Burnley, 1989). In one of these samples (BS_3_1073 in Incel et al. 2017), garnet grains that are cut and displaced by the faults show microstructures similar to what has been described from 'pulverized' garnets in natural fault rocks from lower crustal lithologies (Austrheim et al., 2017; Petley-Ragan et al., 2018). Here, we further investigate the micro- and nanostructure of different garnets found in this sample. In addition, we model the spatial relation of the occurrence and absence of garnet fracturing relying on linear elastic fracture mechanics with the aim to gain further insight into the nucleation and failure mechanisms of intermediate-depth earthquakes.

2. Experimental methods and analytical techniques

2.1 Sample description and preparation of the starting material

A lawsonite-bearing blueschist from Alpine Corsica served as sample material. To avoid any initial texture of the starting material a chemically homogeneous part of this blueschist was crushed and sieved to a grain size <38 μm. The major phases are glaucophane and lawsonite in a ratio of ~3:2 making up ~90 vol.% of the powder. Minor and accessory phases are garnet, omphacite, actinolite, titanite, and phengite. The blueschist powder was hot-pressed at 3 GPa and 923 K for 24 hours in a piston-cylinder and machined to approx. 2.1 mm in diameter and 3 mm in height. After hot-pressing, the sample's phases reveal a

homogeneous texture (Fig. 1a). In particular, the garnets are randomly distributed throughout the sample as evidenced by the Mn-element distribution map (Fig. 1b).

2.2 D-DIA deformation experiment

A 9×9×8 mm sized amorphous Boron-epoxy cuboid was used as pressure medium for the experiment performed using a D-DIA apparatus. The hot-pressed sample is located in the middle of this cuboid, sandwiched between two gold foils and two alumina pistons, and surrounded by a BN sleeve that is inserted into a graphite furnace.

The deformation apparatus is mounted on the GSECARS beamline at the Advanced Photon Source, National Laboratory, Argonne, IL, USA. The use of synchrotron radiation during deformation made it possible to calculate the differential stress as well as the strain and the strain rate during deformation. Stress was calculated on lattice planes of glaucophane using powder diffraction patterns that were taken every five minutes of the deforming sample and the strain was measured by using radiographs of the sample that were also taken every five minutes during deformation. Details of the stress and strain calculation are described by Incel et al. (2017). Additionally, the D-DIA apparatus is equipped with an acoustic emission (AE) system. Acoustic emissions were recorded using a sampling rate of 50 MHz and in trigger mode with a trigger threshold of 250 mV on two channels. The duration of the largest AEs recorded were in the range of a few hundred microseconds. Hence, the interval size over which the stress measurements are made is around six magnitudes larger than the event duration. Further details on the experimental and AE setup can be found in Wang et al. (2003), Gasc et al. (2011), and Schubnel et al. (2013).

First, the sample assembly was loaded hydrostatically to a confining pressure (P_c) of 3 GPa (here confining pressure P_c equals the least principal stress σ_3). Then, heating was initialized by increasing the furnace power manually to reach a temperature of 583 K. The sample was kept at these conditions for 30 min before deformation with a strain rate of approx. 5×10^{-5} s^{-1}

commenced. While deformation of the sample proceeded, the power was increased in 10 W steps to heat up the sample from initially 583 to 1073 K. Heating steps were initiated at 5, 12, 18, 20, 25, 30, and 35 % axial strain.

2.3 Analytical techniques

Microstructural analyses of the recovered sample were performed using a field-emission scanning electron microscope (FE-SEM) with an acceleration voltage of 15 kV. To investigate the nanostructure of this sample, three focused-ion beam (FIB) sections were cut using a FEI-Helios G4 UC-Dual Beam system for imaging, analysis and transmission electron microscopy (TEM). The nanostructural analyses were conducted using a FEI Tecnai TEM and a Jeol JEM 2011 transmission electron microscope. For both machines, the acceleration voltage was 200 keV.

3. Results

3.1 Mechanical data and acoustic emissions

During the first stage of deformation at a temperature of 583 K, the sample was strained by 5 % and the differential stress increased towards a peak stress of approx. 3 GPa, i.e. the level of the confining pressure (Fig. 2). The differential stress decreased continuously during syndeformational heating of the sample. A total axial strain of 40 % was accumulated by the time the temperature reached 1073 K. In total 10 acoustic emissions were recorded between 10 to 19 % axial strain. Two events recorded at around 12 % and at approx. 19 % axial strain, respectively, were large events almost reaching voltage saturation of the recording system (5 V).

141 3.2 Microstructural analyses

142 Microstructural investigations using the field-emission scanning electron microscope (FE-
143 SEM) revealed faults oriented at an angle of around 45° to the direction of the axial stress σ_1
144 crosscutting the entire sample (Fig. 3a). It is possible that either some of the fault-filling
145 material (gouge) of the major faults was lost during sample preparation or the fault surfaces
146 were separated during decompression. However, some relicts of gouge material are preserved
147 at the fault borders. These relicts show holes after interaction with the electron beam of the
148 SEM, implying that this material is poorly crystalline (Fig. 3c).

149 Two different types of garnets can be identified in the deformed sample, (i) garnet crystals
150 that are dissected and displaced along narrow faults (<1 μm wide; Figs. 3c; 4a-c) and (ii)
151 unsheared garnet grains situated at some distance to the nearest fault (~0.5 to 1.5 mm; Figs.
152 3b, 4d, e). Two example sets of displaced garnet parts show apparent shear displacements of
153 42 and 58 μm, respectively (Figs. 3c; 4a). Back-scattered electron (BSE) imaging reveals that
154 the displaced garnet halves are fragmented into pieces with diameters <1 μm (Figs. 3d; 4b)
155 and some of them were dragged along during slip (red arrow in Fig. 3d). Garnet grains located
156 further away from the fractures do not seem to be fragmented at this magnification in the
157 SEM (Figs. 3b; 4d, e).

158 3.3 Nanostructural analyses

159 Transmission electron microscope (TEM) analyses were performed at three different sites
160 (Fig. 3b, c) to investigate the nanometer-scale structures of: (i) the fault-gouge of the narrow
161 fault dissecting and displacing a garnet crystal, (ii) a garnet crystal that is cut by this narrow
162 fault, hereafter referred to as damage-zone garnet, and (iii) a garnet crystal located at a
163 minimum of ~0.5 mm from any fault, denoted as host-rock garnet. The fault-gouge contains
164 garnet crystals with sizes ranging from <20 nm to ~100 nm. In bright field mode TEM

images, the material embedding the garnets appeared brighter than the garnet grains (Fig. 5a). An electron diffraction pattern of this area showed a few diffraction spots but also a diffuse halo (Fig. 5b) implying a combination of domains that have lost their long-range crystalline order and crystals large enough to produce diffraction spots.

Scanning transmission electron microscopy (STEM) of the damage-zone garnet demonstrates that this grain is completely shattered into small fragments (Figs. 5c, 6a) surrounded by a fault-filling material exhibiting vesicles and idiomorphic crystals (Fig. 6a). Using energy-dispersive spectroscopy (EDS) measurements these idiomorphic crystals were identified as omphacite. The surrounding matrix mainly consists of Si, Al, Na, and Ca in addition to O. The diffraction pattern obtained from a circular area with a diameter of ~500 nm in the shattered damage-zone garnet shows few large and several weak diffraction spots, indicative of a polycrystalline material, together with a diffuse halo in its center (Fig. 5c, d). This halo is less prominent than the one obtained from diffraction of the fault-gouge (Fig. 5b). A bright field and a dark field mode image of the same area within the shattered damage-zone garnet taken at high magnification document grain-size and crystal-orientation variation, respectively (Fig. 6b, c). The bright field image shows several grains ranging in size from ~10 to ~50 nm in diameter (Fig. 6b). A quantitative determination of the grain-size distribution is hampered by the abundant overlap of small grains. Lattice fringes are clearly visible locally (Fig. 6c). However, the brightness variation in the corresponding dark-field mode image suggests variable lattice orientation on the nanometer scale.

Nanostructural analysis of the host-rock garnet shows numerous fracture-like features and possibly subgrains ranging in diameter from several hundred nanometers to ~5 µm (Fig. 5e). In contrast to the damage-zone garnet, though, very few grains have diameters <100 nm (Fig. 5c, e). A diffraction pattern of an area with a diameter of ~500 nm (Fig. 5e) indicates a high degree of crystallinity in this zone (Fig. 5f).

4. Discussion

4.1 Garnet pulverization due to dynamic rupture propagation

Our microscopic analyses revealed extensive fragmentation and grain-size reduction of the damage-zone garnet. Its diffraction pattern shows numerous weak diffraction spots indicating the presence of many small crystals. Additionally, a diffuse halo is observed implying that some subdomains are either amorphous or too small (<10 nm) to produce well-defined diffraction spots (Fig. 6c; Yund et al., 1990). On the contrary, the host-rock garnet is fully crystalline and mainly reveals subgrain-formation (Fig. 5e, f). These experimental microstructures are strikingly similar to what Austrheim et al. (2017) described as "pulverization structures" in garnets found in close vicinity to a pseudotachylyte produced during coseismic loading and faulting of granulites from the Bergen Arcs, Norway, and to those found in garnets from mylonitic micaschists in the Sesia Zone, Swiss Alps (Trepmann and Stöckhert, 2002).

Based on the record of acoustic emissions (Fig. 2), faulting and associated pulverization of the wall rock occurred at a confining pressure of ~3 GPa, a differential stress of ~2.5 GPa, in a temperature range from 640 to 720 K, at an experimentally imposed strain rate of 5×10^{-5} s^{-1} and at ~10 to 19 % axial strain. One characteristic feature of pulverized structures is the absence or the low amount of shearing of the fragments (Trepmann and Stöckhert, 2002; Austrheim et al., 2017). Due to the small fragment sizes of the damage-zone garnet it was not possible to measure their orientation. It is likely that the fragments experienced some shearing during further deformation as evidenced by the 'tailing' of the damage-zone garnet into the fault (red arrow in Fig. 3d). However, because the fragments' arrangement still mimics a typical garnet crystal shape we can exclude significant shearing of the bulk crystals and their environment (Figs. 3c, 4a, 5c). As evidenced by the microstructure of the recovered sample

showing lawsonite pseudomorphs as well as by in-situ monitoring of the mineral assemblage during deformation, extensive reaction comprising the dehydration of lawsonite took place at a later stage during deformation (Incel et al., 2017). Therefore, most of the remaining strain was accommodated by lawsonite dehydration involving a solid volume change of around -20 %.

When occurring at upper crustal depth (<15 km), wall-rock damage is explained by high strain rates and stresses around a dynamically propagating rupture tip (Reches and Dewers, 2005; Dor et al., 2006; Doan and Gary, 2009; Mitchell et al., 2011; Bhat et al., 2012; Rempe et al., 2013; Aben et al., 2017a, 2017b, 2016; Xu and Ben-Zion, 2017; Griffith et al., 2018). Due to the much lower strength of rocks in tension than in compression, recently published studies highlight the impact of isotropic or quasi-isotropic tension on the pulverization of rocks (Xu and Ben-Zion, 2017; Griffith et al., 2018). In the model of Grady (1982) the author quantifies the relation between the energy needed to create new fracture surfaces during fragmentation and the inertial or kinetic energy available due to rapid loading. Later Glenn and Chudnovsky (1986) added a strain energy term to this model that accounts for the energy consumed by the solid until reaching its tensile strength. Based on this model, fragment size will not vary over a wide range of strain rates (strain energy dominated regime). Once the tensile strength of the material is exceeded, the fragment size exponentially decays with increasing strain rate (kinetic energy dominated; Grady, 1982). Across natural faults, this situation is realized in close distance (~5 cm) to the fault plane where strain rates are expected to be high (Griffith et al. 2018). In the present study, we follow a similar approach as presented in Griffith et al. (2018) in order to investigate, if the above model can explain the observed difference in fragmentation intensity between the damage-zone and the host-rock garnet. First, we check if the calculated fragment size matches our measured garnet fragments using the Glenn and Chudnovsky (1986) model. Then, we test if the corresponding strain rates

239 fit the predicted strain rates around a dynamically propagating mode II crack tip at the
240 respective positions of the damage-zone and the host-rock garnet using linear elastic fracture
241 mechanics (see Freund, 1990). For these calculations, we used a density ρ= 3,000 kg m^{-3}, a
242 garnet fracture toughness K_{IC}= 1.5 MPa (Mezeix and Green, 2006), and a range in garnet
243 tensile strength σ*= 433 MPa to 4.3 GPa deduced using reported single crystal or aggregate
244 compressive strengths (Pardavi-Horváth, 1984; Kavner, 2007) assuming that the tensile
245 strength of a solid is around a third of its compressive strength. We used a shear modulus μ=
246 64 GPa for glaucophane (Bezacier et al., 2010), a Poisson's ratio υ= 0.22 (Cao et al., 2013),
247 and two different rupture velocities $v_r = 0.8c_s$ and $v_r = 0.9c_s$ with c_s being the shear wave
248 speed. The microstructural observations indicate a coseismic slip of a few tens of micrometer
249 (Figures 3c; 4a) corresponding to a range in fracture energy G_c of ~0.1 to 100 J m^{-2}
250 (Passelègue et al., 2016), deduced from experiments accounting for the uncertainty regarding
251 the critical slip distance (further explanations in Passelègue et al., 2016).
252 The calculated fragment size distribution matches quite well the measured garnet
253 fragments of the host-rock and the damage-zone garnet, respectively (Figures 5; 7a). Based on
254 linear elastic fracture mechanics, strain rates at the position of the host-rock garnet range from
255 ~10^2 to ~10^4 s^{-1} (Figure 7b). Combining the results of both calculations, the host-rock garnet
256 plots within the strain energy dominated regime (Figure 7). This fits well the nanostructural
257 analysis that reveals some fracture-like features, but mostly polygons that are homogeneously
258 sized resembling subgrains (Figures 5e; 8b). To explain the extensive fragmentation of the
259 damage-zone garnet, strain rates must have been high enough to exceed garnet's tensile
260 strength. Based on the measured fragment sizes of the damage-zone garnet, strain rates have
261 to be at least 10^8 s^{-1} (Figure 7a). Since the crack tip passed through this garnet crystal, such
262 high strain rates are realized within the damage-zone garnet volume in close vicinity to the
263 rupture tip (Figures 7b; 8a, b).

The theory of linear elastic fracture mechanics provides an asymptotic solution for a semi-infinite crack that is only valid in the near-tip field (Freund, 1990). This requirement is obviously difficult to satisfy regarding the length ratio of the shear fracture relative to the respective garnet distances to the fault plane. A previous theoretical study on the relation between wall-rock damage and depth reports an increase in the amount of fracture energy dissipated in the off-fault medium with increasing depth (Okubo et al., 2019). The authors also state that the width of the damage-zone decreases with depth. Consequently, this implies that at deeper depth the off-fault damage will be confined to a narrow zone around the fault. Showing extensivly damaged garnets only in close vicinity to the fault, our experimental study confirms these theoretical results.

4.2 Frictional melting of blueschist

Sliding of the fracture surfaces in mode II causes a temperature increase, which may eventually lead to melting of the fracture surfaces. We deduce the presence of a solidified melt from the amorphous material present in the fault-filling material (Fig. 5a,b) and in some places intruded the shattered damage-zone garnet (Fig. 6a). In this "melting scenario", the vesicles in the amorphous material reflect fluid exsolution during decompression of the melt and the observed idiomorphic omphacite crystals nucleate and grow during cooling of the melt (Fig. 6a). Assuming a wet basalt solidus temperature T_s of ~1,000 K at ~3 GPa (Hacker et al., 2003a), a sliding-related increase in temperature of 280-360 K over the temperatures prevailing during the AE activity (640-720 K) would be sufficient to cause local melting. After Cardwell et al. (1978), the temperature rise ΔT on a slipping fault can be expressed as

$$\Delta T = \frac{\tau D}{\rho c_p \sqrt{\pi \kappa t_{\text{slip}}}} \quad \text{(eq. 1)}$$

with shear stress τ, shear displacement D, density ρ, specific heat capacity c_p (1,100 J kg^{-1} K^{-1} at ~1,000 K; Hartlieb et al., 2016), thermal diffusivity κ (~10^{-6} m s^{-1}), and slip duration t_{slip}.

The nominal shear stress τ and normal stress σ_n acting on the fault are ~1.25 GPa and 4.25 GPa, respectively (with $\theta \approx 45°$, $\sigma_1 = 5.5$ GPa, and $\sigma_3 = 3$ GPa). Assuming a minimum total displacement $D = 42$ μm (Figs. 3c) and only 10 % of that slip to have happened coseismically and a sliding velocity of ~1 m s^{-1} (for a crack-like rupture; Schubnel et al., 2013) gives a slip duration t_{slip} of ~4.2×10^{-6} s. These estimates result in a ΔT of >390 K indeed exceeding the difference between prevailing assembly temperature and the sample's solidus temperature.

The presence of a melt film on the fault surfaces can lead to fault lubrication (Di Toro et al., 2006). Dynamic shear strength τ_f of a fault with a continuous melt film strongly depends on the ratio between the width w of the molten zone that is filling the fault plane and the slip displacement (e.g., Ferrand et al., 2018)

$$\tau_f = \frac{\rho[H + c_p \Delta T]w}{(1-\eta)D} \quad \text{(eq. 2)}$$

with the latent heat of fusion H (≈ 3×10^5 J K^{-1}) and the radiative efficiency η. In our sample, the narrow fault that contains molten material shows a width of $w \approx$ 100-500 nm. Previous studies showed that the seismic efficiency, as function of the mechanical energy spent on slip during rupture, ranges between $0.1 < \eta < 0.5$ (Poli and Prieto, 2016). Within this span, equation (2) gives a dynamic shear strength of the fault as low as ~7 to 66 MPa (Fig. 9a) corresponding to friction coefficients of ~0.002 to 0.015 (Fig. 9b), i.e., significant lubrication (Figure 8c).

5. Conclusion and implications

The micro- and nanostructures observed in the damage-zone garnet, which resemble pulverization structures in natural rocks at upper as well as at lower crustal depths, can be explained by extensive fragmentation due to high strain rates associated with a dynamically propagating shear fracture. Such microstructures are not, however, compatible with fault models that involve failure by self-localizing thermal runaway mechanisms. In such a

situation, one would expect to see evidence of pre-failure shear strain in the wall rocks, and the local differential stress levels should not rise above the initial externally imposed far-field stress (John et al., 2009). However, it has been demonstrated that high local stresses, e.g., due to coseismic loading, are required to fracture garnet (Trepmann and Stöckhert, 2002). After the passage of the crack tip, frictional sliding of the fault surfaces causes melting and fault lubrication. Our experimental study emphasizes the importance of dynamic rupture as a brittle precursor to unstable frictional slip even at upper mantle depths.

Acknowledgements

The authors thank the two reviewers Greg Hirth and Ashley Griffith for their comments and suggestions that helped improving the manuscript. The authors also thank Anja Schreiber for the preparation of the FIB sections and Christian Chopin who provided the blueschist sample. Special thanks to Frans Aben, François Passelègue, and Yehuda Ben-Zion for their help and discussions and to Paul Meakin for a careful review of an early version of the manuscript. The study received funding from the Alexander von Humboldt-foundation (Feodor Lynen-fellowship to S.I.) and support from Geo.X in form of a travel Grant (to S.I.). Further funding came from the People Program (Marie Curie Actions) of the European Union's Seventh Framework Program FP7/2017-2013/ and Horizon 2020 under REA grant agreements n° 604713 (to A.S.) and n° 669972 (to B.J.), EAR-1661489 for the development of AE experiments (Y.W.). This research used resources of the Advanced Photon Source, a U.S. Department of Energy Office of Science User Facility operated by Argonne National Laboratory (contract n° DE-AC02-06CH11357). Financial support for H.M.F through funding provided by the German Helmholtz Recruiting Initiative (award number I-044-16-01) to Liane G. Benning from the GFZ is acknowledged.

334 **References**

335 Aben, F.M., Doan, M., Mitchell, T.M., Toussaint, R., Reuschlé, T., Fondriest, M., Gratier, J.,
336 Renard, F., 2016. Dynamic fracturing by successive coseismic loadings leads to
337 pulverization in active fault zones 121, 2338–2360. doi:10.1002/2015JB012542

338 Aben, F.M., Doan, M.L., Gratier, J.P., Renard, F., 2017a. AGU Monograph - Fault Zone
339 Dynamic Processes: Evolution of Fault Properties During Seismic Rupture, 1st ed,
340 Current. John Wiley & Sons, Inc.

341 Aben, F.M., Doan, M.L., Gratier, J.P., Renard, F., 2017b. High strain rate deformation of
342 porous sandstone and the asymmetry of earthquake damage in shallow fault zones. Earth
343 Planet. Sci. Lett. 463, 81–91. doi:10.1016/j.epsl.2017.01.016

344 Angiboust, S., Agard, P., Yamato, P., Raimbourg, H., 2012. Eclogite breccias in a subducted
345 ophiolite: A record of intermediatedepth earthquakes? Geology 40, 707–710.
346 doi:10.1130/G32925.1

347 Austrheim, H., Dunkel, K.G., Plümper, O., Ildefonse, B., Liu, Y., Jamtveit, B., 2017.
348 Fragmentation of wall rock garnets during deep crustal earthquakes. Sci. Adv. 3, 1–7.
349 doi:10.1126/sciadv.1602067

350 Ben-Zion, Y., 2003. Appendix 2, Key Formulas in Earthquake Seismology. Int. Handb.
351 Earthq. Eng. Seismol. Part B, 1857–1875.

352 Bezacier, L., Reynard, B., Bass, J.D., Wang, J., Mainprice, D., 2010. Elasticity of
353 glaucophane, seismic velocities and anisotropy of the subducted oceanic crust.
354 Tectonophysics 494, 201–210. doi:10.1016/j.tecto.2010.09.011

355 Bhat, H.S., Rosakis, A.J., Sammis, C.G., 2012. A Micromechanics Based Constitutive Model
356 for Brittle Failure at High Strain Rates. J. Appl. Mech. 79, 31016.
357 doi:10.1115/1.4005897

358 Braeck, S., Podladchikov, Y.Y., 2007. Spontaneous thermal runaway as an ultimate failure

359 mechanism of materials. Phys. Rev. Lett. 98. doi:10.1103/PhysRevLett.98.095504
360 Cao, Y., Jung, H., Song, S., 2013. Petro-fabrics and seismic properties of blueschist and
361 eclogite in the North Qilian suture zone, NW China: Implications for the low-velocity
362 upper layer in subducting slab, trench-parallel seismic anisotropy, and eclogite
363 detectability in the subduction z. J. Geophys. Res. Solid Earth 118, 3037–3058.
364 doi:10.1002/jgrb.50212
365 Cardwell, R.K., Chinn, D.S., Moore, G.F., Turcotte, D.L., 1978. Frictional Heating on a Fault
366 Zone With Finite Thickness. Geophys. J. R. Astron. Soc. 52, 525–530.
367 doi:10.1111/j.1365-246X.1978.tb04247.x
368 Deseta, N., Ashwal, L.D., Andersen, T.B., 2014. Initiating intermediate-depth earthquakes:
369 Insights from a HP-LT ophiolite from Corsica. Lithos 206–207, 127–146.
370 doi:10.1016/j.lithos.2014.07.022
371 Di Toro, G., Hirose, T., Nielsen, S., Pennacchioni, G., Shimamoto, T., 2006. Natural and
372 Experimental Evidence During Earthquakes. Science (80-.). 311, 647–649.
373 doi:10.1126/science.1121012
374 Doan, M.L., Gary, G., 2009. Rock pulverization at high strain rate near the SanAndreas fault.
375 Nat. Geosci. 2, 709–712. doi:10.1038/ngeo640
376 Dobson, D.P., Meredith, P.G., Boon, S.A., 2002. Simulation of subduction zone seismicity by
377 dehydration of serpentine. Science (80-.). 298, 1407–1410.
378 doi:10.1126/science.1075390
379 Dor, O., Ben-Zion, Y., Rockwell, T.K., Brune, J., 2006. Pulverized rocks in the Mojave
380 section of the San Andreas Fault Zone. Earth Planet. Sci. Lett. 245, 642–654.
381 doi:10.1016/j.epsl.2006.03.034
382 Ferrand, T.P., Hilairet, N., Incel, S., Deldicque, D., Labrousse, L., Gasc, J., Renner, J., Wang,
383 Y., Green, H.W., Schubnel, A., 2017. Dehydration-driven stress transfer triggers

intermediate-depth earthquakes. Nat. Commun. 8, 1–11. doi:10.1038/ncomms15247

Ferrand, T.P., Labrousse, L., Eloy, G., Fabbri, O., Hilairet, N., Schubnel, A., 2018. Energy balance from a mantle pseudotachylyte, Balmuccia, Italy. J. Geophys. Res. Solid Earth. doi:10.1002/2017JB014795

Freund, L.B., 1990. Dynamic Fracture Mechanics, Cambridge University Press. doi:10.1017/CBO9780511546761

Gasc, J., Hilairet, N., Yu, T., Ferrand, T., Schubnel, A., Wang, Y., 2017. Faulting of natural serpentinite: Implications for intermediate-depth seismicity. Earth Planet. Sci. Lett. 474, 138–147. doi:10.1016/j.epsl.2017.06.016

Gasc, J., Schubnel, A., Brunet, F., Guillon, S., Mueller, H.J., Lathe, C., 2011. Simultaneous acoustic emissions monitoring and synchrotron X-ray diffraction at high pressure and temperature: Calibration and application to serpentinite dehydration. Phys. Earth Planet. Inter. 189, 121–133. doi:10.1016/j.pepi.2011.08.003

Glenn, L.A., Chudnovsky, A., 1986. Strain-energy effects on dynamic fragmentation. J. Appl. Phys. 59, 1379–1380.

Grady, D.E., 1982. Local inertial effects in dynamic fragmentation. J. Appl. Phys. 53, 322–325. doi:10.1063/1.329934

Green II, H.W., Burnley, P.C., 1989. A new self-organizing mechanism for deep-focus earthquakes. Nature 341, 733–737. doi:10.1038/341733a0

Griffith, W.A., St. Julien, R.C., Ghaffari, H.O., Barber, T.J., 2018. A Tensile Origin for Fault Rock Pulverization. J. Geophys. Res. Solid Earth 123, 7055–7073. doi:10.1029/2018JB015786

Guermani, A., Pennacchioni, G., 1998. Brittle precursors of plastic deformation in a granite: an example from the Mont Blanc massif (Helvetic, western Alps). J. Struct. Geol. 20, 135–148. doi:10.1016/S0191-8141(97)00080-1

409 Hacker, B.R., Abers, G.A., Peacock, S.M., 2003a. Subduction factory 1. Theoretical
410 mineralogy, densities, seismic wave speeds, and H $_2$ O contents. J. Geophys. Res. Solid
411 Earth 108, 1–26. doi:10.1029/2001JB001127
412 Hacker, B.R., Peacock, S.M., Abers, G.A., Holloway, S.D., 2003b. Subduction factory 2. Are
413 intermediate-depth earthquakes in subducting slabs linked to metamorphic dehydration
414 reactions? J. Geophys. Res. Solid Earth 108. doi:10.1029/2001JB001129
415 Hartlieb, P., Toifl, M., Kuchar, F., Meisels, R., Antretter, T., 2016. Thermo-physical
416 properties of selected hard rocks and their relation to microwave-assisted comminution.
417 Miner. Eng. 91, 34–41. doi:10.1016/j.mineng.2015.11.008
418 Incel, S., Hilairet, N., Labrousse, L., John, T., Deldicque, D., Ferrand, T.P., Wang, Y.,
419 Morales, L., Schubnel, A., 2017. Laboratory earthquakes triggered during eclogitization
420 of lawsonite-bearing blueschist. Earth Planet. Sci. Lett. 459, 320–331.
421 doi:10.1016/j.epsl.2016.11.047
422 Incel, S., Labrousse, L., Hilairet, N., John, T., Gasc, J., Shi, F., Wang, Y., Andersen, T.B.,
423 Renard, F., Jamtveit, B., Schubnel, A., 2019. Reaction-induced embrittlement of the
424 lower continental crust. Geology 47, 235–238. doi:https://doi.org/10.1130/G45527.1
425 John, T., Medvedev, S., Rüpke, L.H., Andersen, T.B., Podladchikov, Y.Y., Austrheim, H.,
426 2009. Generation of intermediate-depth earthquakes by self-localizing thermal runaway.
427 Nat. Geosci. 2, 137–140. doi:10.1038/ngeo419
428 Kavner, A., 2007. Garnet yield strength at high pressures and implications for upper mantle
429 and transition zone rheology. J. Geophys. Res. Solid Earth 112, 1–9.
430 doi:10.1029/2007JB004931
431 Kelemen, P.B., Hirth, G., 2007. A periodic shear-heating mechanism for intermediate-depth
432 earthquakes in the mantle. Nature 446, 787–790. doi:10.1038/nature05717
433 Kirby, S.H., 1987. Localized polymorphic phase transformations in high-pressure faults and

applications to the physical mechanism of deep earthquakes. J. Geophys. Res. Solid Earth 92, 13789–13800. doi:10.1029/JB092iB13p13789

Kirkpatrick, J.D., Rowe, C.D., 2013. Disappearing ink: How pseudotachylytes are lost from the rock record. J. Struct. Geol. 52, 183–198. doi:10.1016/j.jsg.2013.03.003

Mancktelow, N.S., 2006. How ductile are ductile shear zones? Geology 34, 345–348. doi:10.1130/G22260.1

McKenzie, D., Brune, J.N., 1972. Melting on Fault Planes During Large Earthquakes. Geophys. J. R. Astron. Soc. 29, 65–78. doi:10.1111/j.1365-246X.1972.tb06152.x

Mezeix, L., Green, D.J., 2006. Comparison of the mechanical properties of single crystal and polycrystalline yttrium aluminum garnet. Int. J. Appl. Ceram. Technol. 3, 166–176. doi:10.1111/j.1744-7402.2006.02068.x

Mitchell, T.M., Ben-Zion, Y., Shimamoto, T., 2011. Pulverized fault rocks and damage asymmetry along the Arima-Takatsuki Tectonic Line, Japan. Earth Planet. Sci. Lett. 308, 284–297. doi:10.1016/j.epsl.2011.04.023

Mitchell, T.M., Faulkner, D.R., 2009. The nature and origin of off-fault damage surrounding strike-slip fault zones with a wide range of displacements: A field study from the Atacama fault system, northern Chile. J. Struct. Geol. 31, 802–816. doi:10.1016/j.jsg.2009.05.002

Okazaki, K., Hirth, G., 2016. Dehydration of lawsonite could directly trigger earthquakes in subducting oceanic crust. Nature 530, 81–84. doi:10.1038/nature16501

Okubo, K., Bhat, H.S., Rougier, E., Marty, S., Schubnel, A., Lei, Z., Knight, E.E., Klinger, Y., 2019. Dynamics, radiation and overall energy budget of earthquake rupture with coseismic off-fault damage. arXiv:1901.01771.

Pardavi-Horváth, M., 1984. Microhardness and brittle fracture of garnet single crystals. J. Mater. Sci. 19, 1159–1170. doi:10.1007/BF01120025

459 Passelègue, F.X., Schubnel, A., Nielsen, S., Bhat, H.S., Deldicque, D., Madariaga, R., 2016.
460 Dynamic rupture processes inferred from laboratory microearthquakes. J. Geophys. Res.
461 Solid Earth 121, 4343–4365. doi:10.1002/2015JB012694
462 Petley-Ragan, A., Dunkel, K.G., Austrheim, H., Ildefonse, B., Jamtveit, B., 2018.
463 Microstructural Records of Earthquakes in the Lower Crust and Associated Fluid-Driven
464 Metamorphism in Plagioclase-Rich Granulites. J. Geophys. Res. Solid Earth 123, 3729–
465 3746. doi:10.1029/2017JB015348
466 Poli, P., Prieto, G.A., 2016. Global rupture parameters for deep and intermediate-depth
467 earthquakes. J. Geophys. Res. Solid Earth 121, 8871–8887. doi:10.1002/2016JB013521
468 Prieto, G.A., Froment, B., Yu, C., Poli, P., Abercrombie, R., 2017. Earthquake rupture below
469 the brittle-ductile transition in continental lithospheric mantle. Sci. Adv. 3, 1–6.
470 doi:10.1126/sciadv.1602642
471 Raleigh, C.B., Paterson, M.S., 1965. Experimental deformation of serpentinite and its tectonic
472 implications. J. Geophys. Res. 70, 3965–3985. doi:10.1029/JZ070i016p03965
473 Reches, Z., Dewers, T.A., 2005. Gouge formation by dynamic pulverization during
474 earthquake rupture. Earth Planet. Sci. Lett. 235, 361–374. doi:10.1016/j.epsl.2005.04.009
475 Rempe, M., Mitchell, T., Renner, J., Nippress, S., Ben-Zion, Y., Rockwell, T., 2013. Damage
476 and seismic velocity structure of pulverized rocks near the San Andreas Fault. J.
477 Geophys. Res. Solid Earth 118, 2813–2831. doi:10.1002/jgrb.50184
478 Schubnel, A., Brunet, F., Hilairet, N., Gasc, J., Wang, Y., Green, H.W., 2013. Deep-focus
479 earthquake analogs recorded at high pressure and temperature in the laboratory. Science
480 (80-.). 341, 1377–1380. doi:10.1126/science.1240206
481 Sibson, R.H., 1975. Generation of Pseudotachylyte by Ancient Seismic Faulting. Geophys. J.
482 R. Astron. Soc. 43, 775–794. doi:10.1111/j.1365-246X.1975.tb06195.x
483 Thielmann, M., Rozel, A., Kaus, B.J.P., Ricard, Y., 2015. Intermediate-depth earthquake

generation and shear zone formation caused by grain size reduction and shear heating. Geology 43, 791–794. doi:10.1130/G36864.1

Trepmann, C.A., Stöckhert, B., 2002. Cataclastic deformation of garnet: A record of synseismic loading and postseismic creep. J. Struct. Geol. 24, 1845–1856. doi:10.1016/S0191-8141(02)00004-4

Wang, Y., Durham, W.B., Getting, I.C., Weidner, D.J., 2003. The deformation-DIA: A new apparatus for high temperature triaxial deformation to pressures up to 15 GPa. Rev. Sci. Instrum. 74, 3002–3011. doi:10.1063/1.1570948

Xu, S., Ben-Zion, Y., 2017. Theoretical constraints on dynamic pulverization of fault zone rocks. Geophys. J. Int. 209, 282–296. doi:10.1093/gji/ggx033

Yund, R.A., Blanpied, M.L., Tullis, T.E., Weeks, J.D., 1990. Amorphous Material in High Strain Experimental Fault Gouges. J. Geophys. Res. 95, 15,589-15,602.

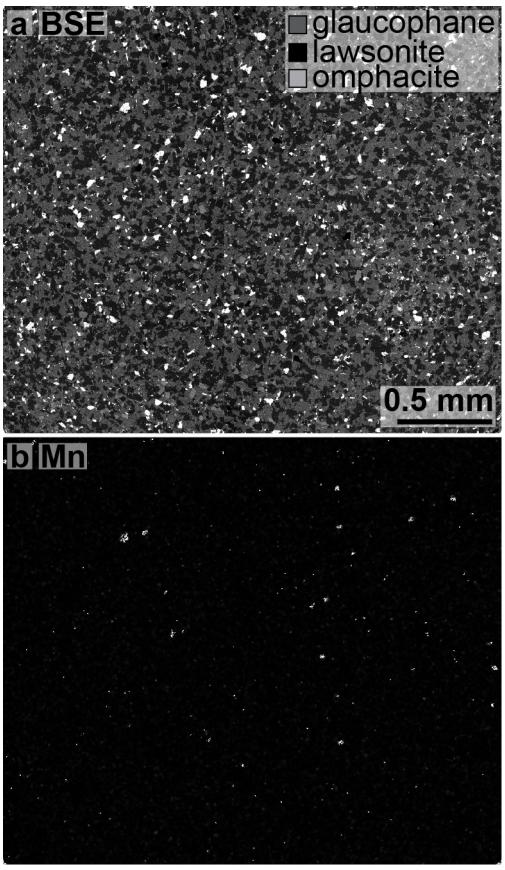

Figure 1: The starting material after hot-pressing. a) Backscattered electron (BSE) image showing that the phases are homogeneously distributed throughout the sample. b) A Mn-distribution map of the same region was used to highlight the location of garnet crystals.

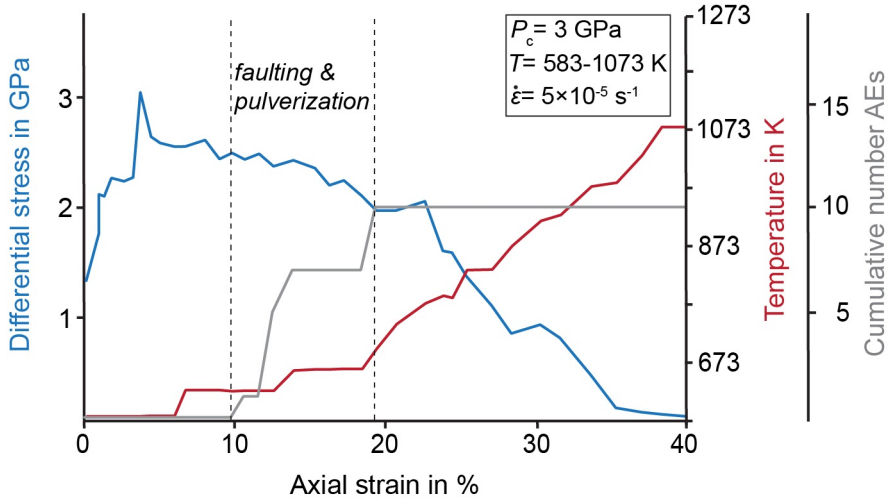

Figure 2: Differential stress, temperature, and cumulative number of acoustic emission (AE) events over axial strain. Based on the record of AEs (grey curve), faulting and pulverization occurs at a confining pressure (P_c)= 3 GPa, a differential stress of ~2.5 GPa (blue curve), in a temperature range of 640 to 720 K (red curve), at an imposed strain rate ($\dot{\varepsilon}$) = 5×10^{-5} s^{-1}, and an axial strain ε= ~10-19 %.

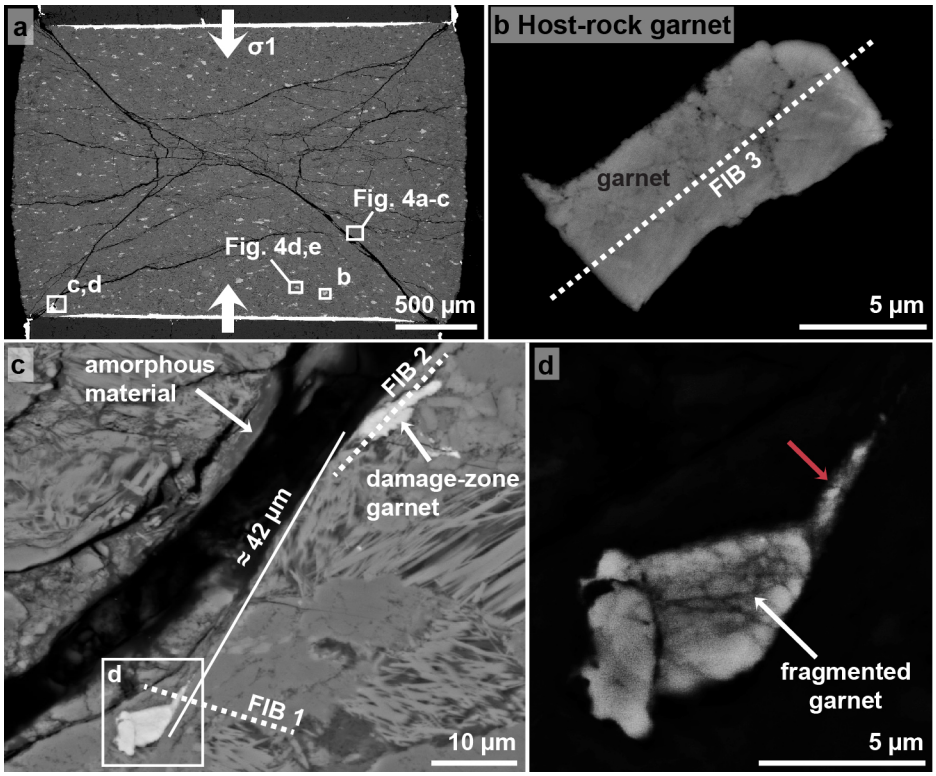

Figure 3: Backscattered electron images of the lawsonite-bearing blueschist sample after deformation. a) Overview image of the sample showing faults oriented at ~45° towards σ_1 crosscutting the sample. The positions of the high-magnification images in b-d as well as the

position for Fig. 4 are highlighted with white rectangles, respectively. b) The host-rock garnet crystal that is located at ~0.5 µm to the closest fault. The location of FIB section 3 is shown as white dashed line. c) A garnet pair that is dissected and displaced along a narrow fault. The apparent displacement is ~42 µm. The locations for FIB sections 1 and 2 are marked by white dashed lines. The white rectangle shows the location of a garnet half presented in d. d) At high magnification and high brightness contrast the garnet half appears fragmented into several pieces < 1µm.

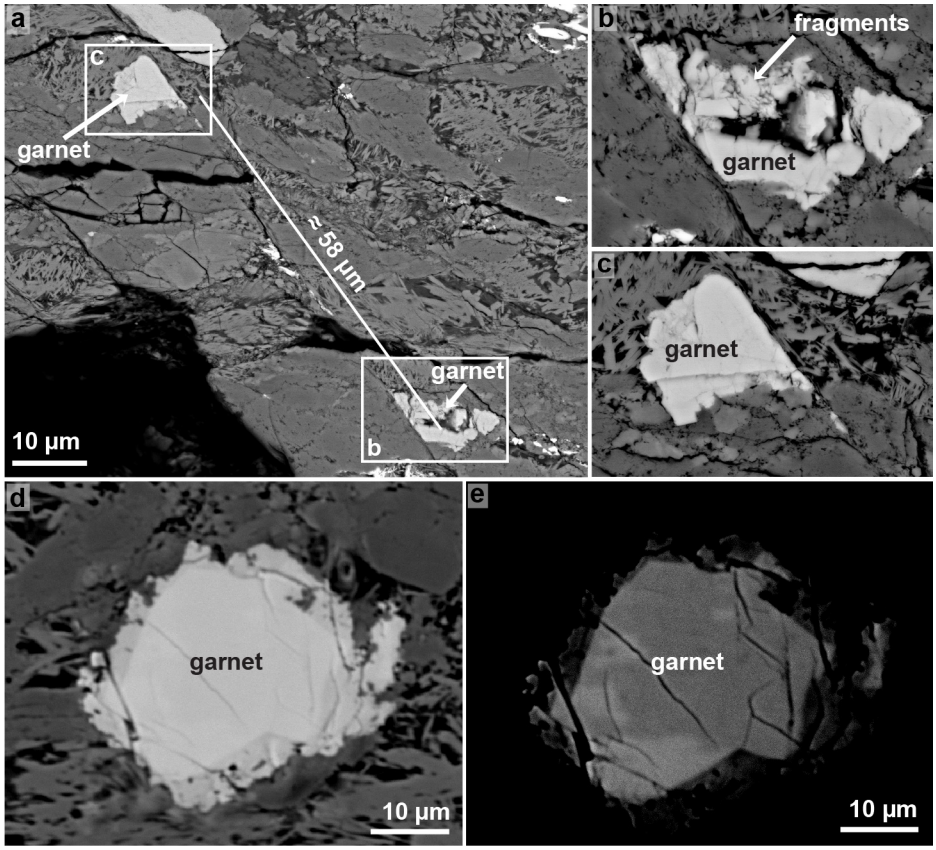

Figure 4: a) Backscattered electron images of another pair of dissected and displaced crystals that are offset by a narrow fault. The offset along the narrow fault is ~58 µm. b and c) The two halves of the garnet pair showing extensive fragmentation in b). d and e) This garnet was found at ~1 mm from the nearest fault and seems relatively intact. e) Same crystal as in d) with the image taken at a higher brightness contrast at the SEM.

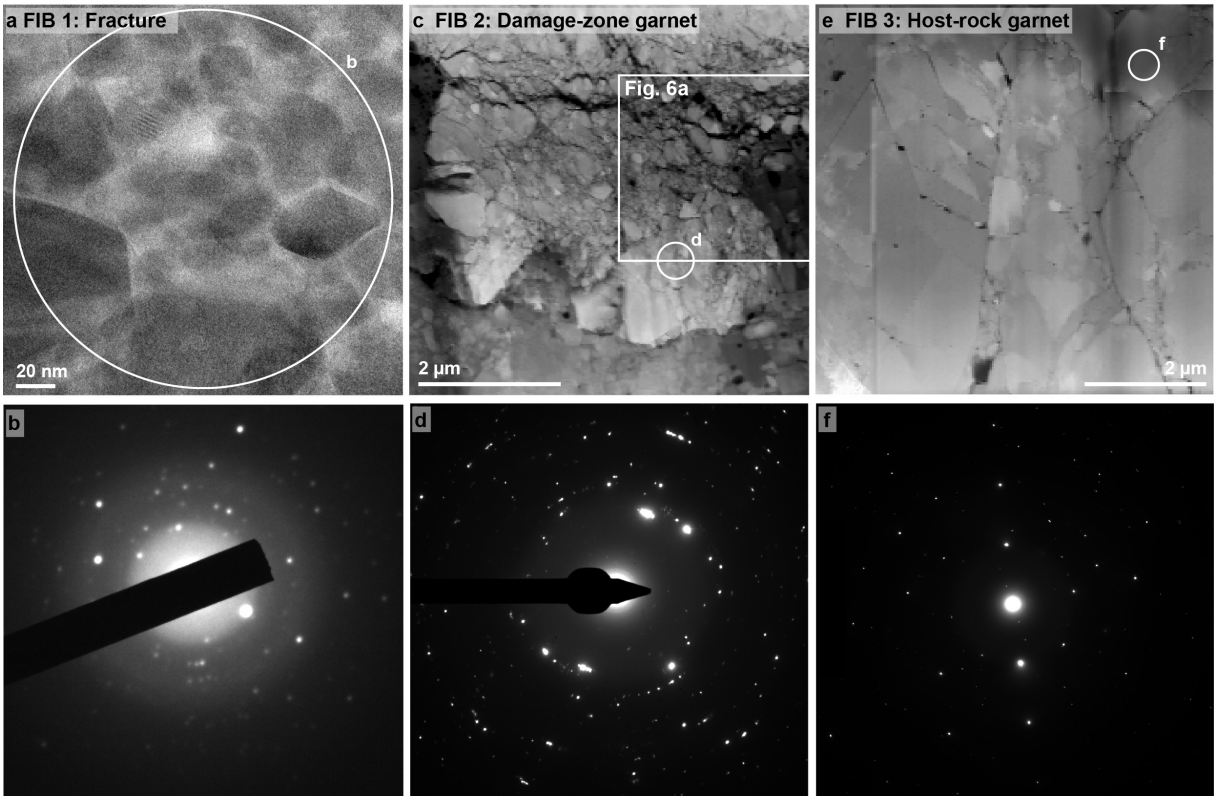

Figure 5: Transmission electron microscope images of the three FIB sections 1-3. a and b) FIB 1 revealing the fault-filling material. a) Bright field image showing dark (i.e. crystalline) garnet crystals floating in a bright (i.e. amorphous) material. The location chosen for a diffraction pattern is highlighted by a white circle. b) Diffraction pattern of the fault-filling material exhibiting few large and several weak diffraction spots and a diffuse halo. c and d) FIB section 2 cut across the damage-zone garnet next to the narrow fault. c) In STEM mode the damage-zone garnet appears to be completely shattered into pieces <1 µm. The white rectangle marks the position of Fig. 6a and the white circle shows the location of the diffraction pattern. d) Diffraction pattern of the shattered damage-zone garnet. Many weak diffraction spots indicate the presence of numerous small crystals. There is also a diffuse halo in the center of the diffraction pattern. e and f) FIB section 3 cut across the relatively intact host-rock garnet located at ~0.5 µm from a fault. e) The fragments are much larger than those found in the damage-zone garnet. The white circle highlights the location chosen for a diffraction pattern. f) The diffraction pattern of the area shown in e) presents a crystalline structure.

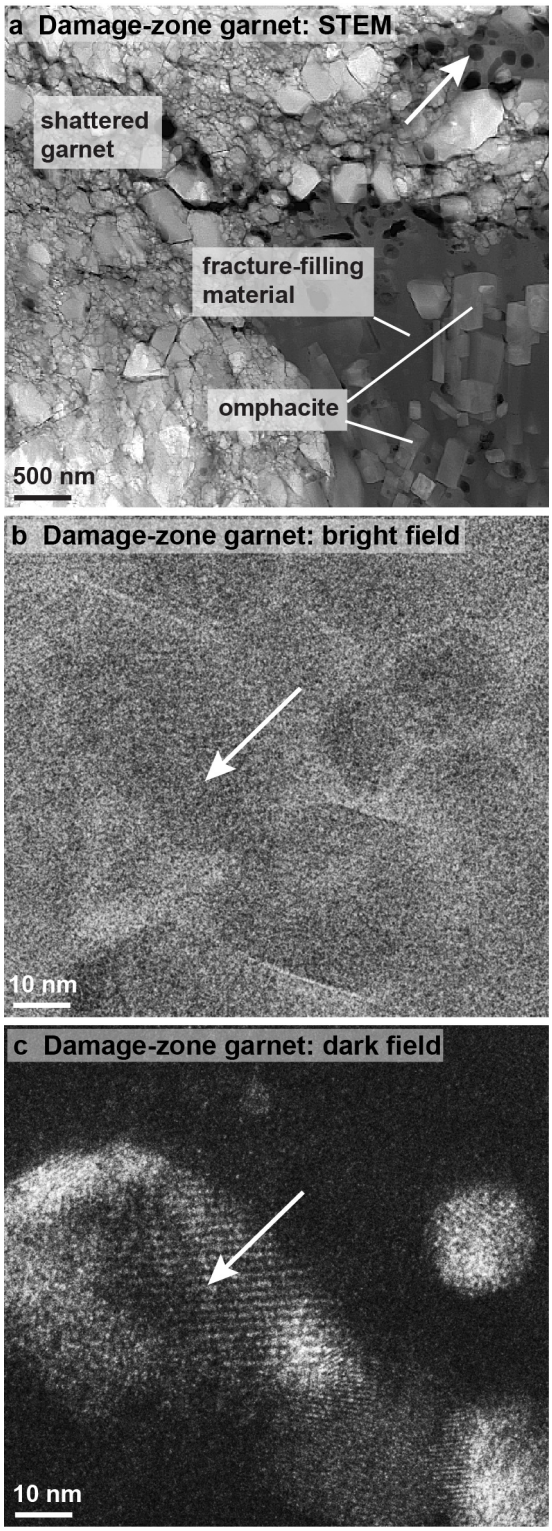

Figure 6: Transmission electron microscopy images of the shattered damage-zone garnet. a) STEM image revealing the fault-filling material surrounding the damage-zone garnet. Within this material vesicles (white arrow) and idiomorphic omphacite crystals can be found. b) Bright field image taken in the same zone as the diffraction pattern (Fig. 5c, d). c) The same area as shown in b) taken in dark field mode. The large grain marked by the white arrow shows subdomains (≤10 nm) that are slightly tilted.

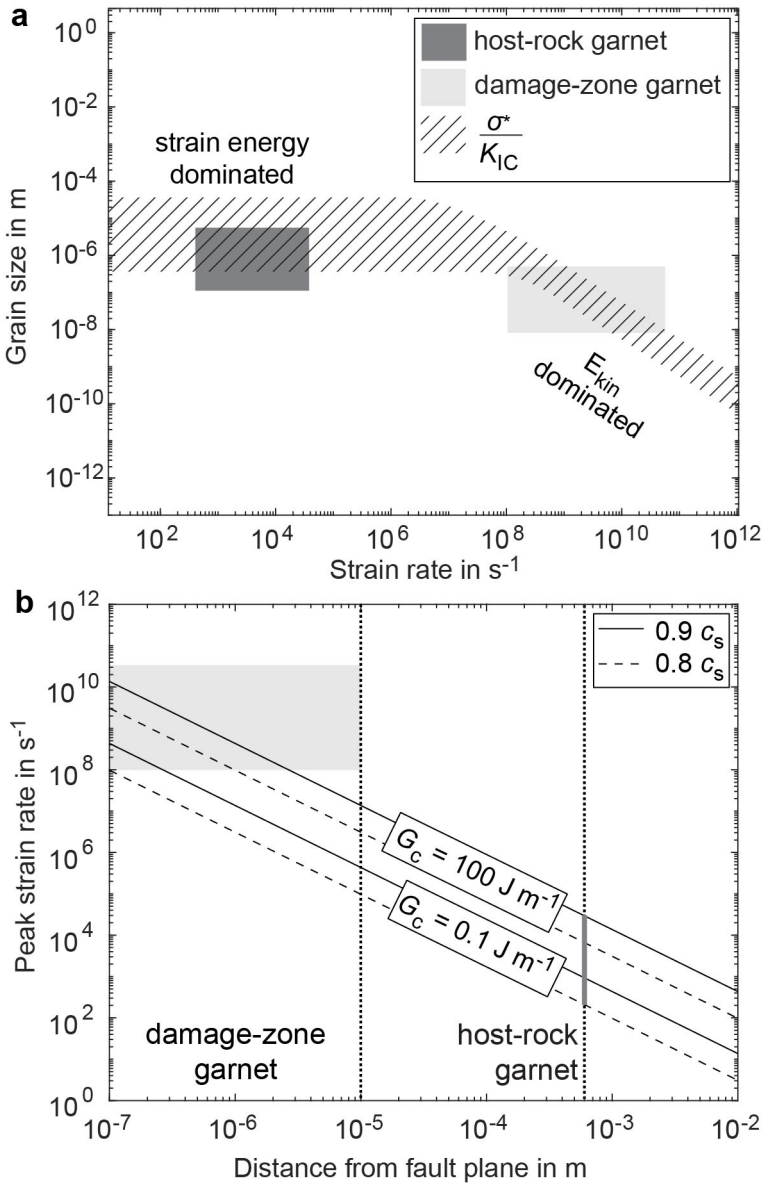

552

553 **Figure 7:** a) Grain size versus strain rate plot based on the models of Grady (1982) and Glenn
554 and Chudnovsky (1986). The measured garnet fragments of the host-rock (dark grey
555 rectangle) and the damage-zone garnet fragments (light grey rectangle) fit quite well the
556 calculated fragment sizes (dashed area) over the investigated strain rate range. The minimum
557 tensile strength for garnet aggregates is 433 MPa deduced from the compressive strength of
558 garnet aggregates under confinement (Kavner, 2007). The maximum tensile strength was
559 deduced from single crystal hardness measurements reported by Pardavi-Horváth (1984). For
560 both we assumed that the tensile strength is around a third of the compressive strength. The
561 fracture toughness of garnet is ~1.5 MPa (Mezeix and Green, 2006). b) Peak strain rates as a
562 function of distance from the fault plane for two different rupture speeds v_r ($0.8c_s$ and $0.9c_s$)
563 and two different fracture energies G_c (0.1 J m^{-1} and 100 J m^{-1}; Passelègue et al., 2016).

564

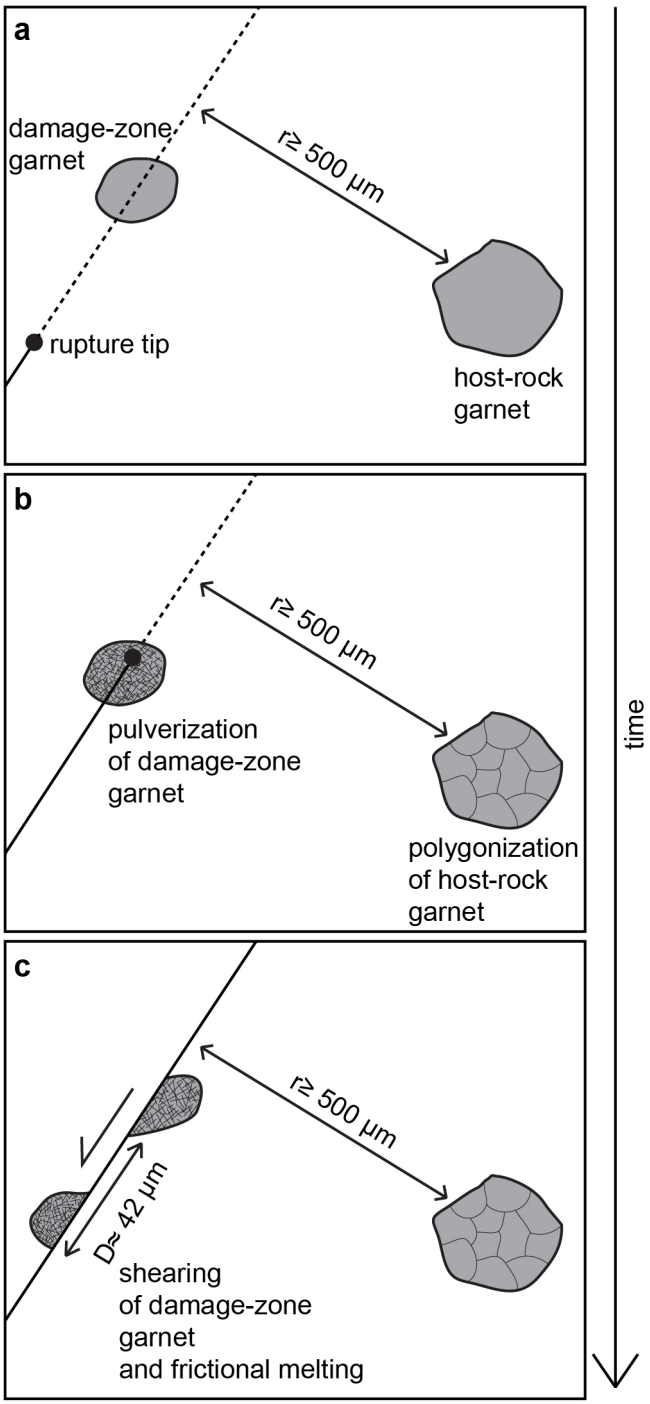

565

566 **Figure 8:** a) Prior to rupture, both garnet crystals are intact. b) The rupture tip passes through
567 the damage-zone garnet. Pulverization of the damage-zone garnet occurs due to the extreme
568 strain rate around the crack tip (E_{kin} dominated Figure 7a). Because strain rate decays with
569 distance, the host-rock garnet that is located at a minimum distance of ~500 µm to the nearest
570 fault only shows the formation of subgrains (strain energy dominated Figure 7a). c) Shearing
571 behind the rupture tip causes the displacement of the garnet halves and eventually frictional
572 melting of the fault surfaces.

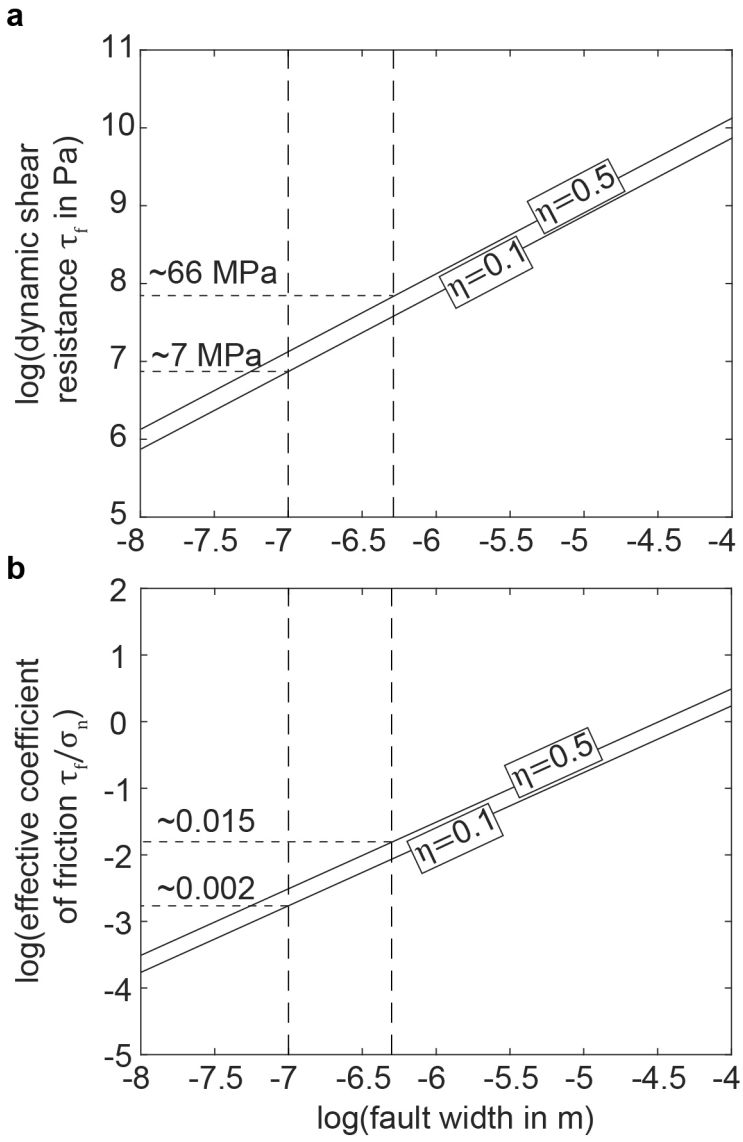

573

574 **Figure 9**: a) Dynamic shear resistance and b) effective coefficient of friction versus width of
575 the slip-associated melt layer. The vertical dashed lines mark the measured width of the
576 molten zone filling out the fault along which a garnet pair is dissected and displaced (Fig. 3c).
577 Recent studies show that the radiative efficiency increases with depth ranging between η= 0.1
578 to 0.5 for intermediate depth earthquakes (50-300 km). The dashed horizontal lines indicate
579 the intercept of this radiative efficiency range and the width range of the molten zone (~100 to
580 500 nm) measured in the sample. The dynamic shear resistance would be ~7 to 66 MPa (a)
581 resulting in an effective coefficient of friction of ~0.002 to 0.015 (b).